Investigation of unsteady, hypersonic, laminar separated flows over a double cone geometry using a kinetic approach

Cite as: Phys. Fluids **30**, 046103 (2018); https://doi.org/10.1063/1.5022598
Submitted: 16 January 2018 . Accepted: 09 March 2018 . Published Online: 02 April 2018

Ozgur Tumuklu, Deborah A. Levin, and Vassilis Theofilis

Investigation of unsteady, hypersonic, laminar separated flows over a double cone geometry using a kinetic approach

Ozgur Tumuklu,[1,a)] Deborah A. Levin,[1,b)] and Vassilis Theofilis[2,c)]
[1]*Department of Aerospace Engineering, University of Illinois at Urbana-Champaign, Urbana, Illinois 61801, USA*
[2]*School of Engineering, University of Liverpool, Liverpool L69 3GH, United Kingdom*

(Received 16 January 2018; accepted 9 March 2018; published online 2 April 2018)

Shock-dominated hypersonic laminar flows over a double cone are investigated using time accurate direct simulation Monte Carlo combined with the residuals algorithm for unit Reynolds numbers gradually increasing from 9.35×10^4 to 3.74×10^5 m^{-1} at a Mach number of about 16. The main flow features, such as the strong bow-shock, location of the separation shock, the triple point, and the entire laminar separated region, show a time-dependent behavior. Although the separation shock angle is found to be similar for all Re numbers, the effects of Reynolds number on the structure and extent of the separation region are profound. As the Reynolds number is increased, larger pressure values in the under-expanded jet region due to strong shock interactions form more prominent λ-shocklets in the supersonic region between two contact surfaces. Likewise, the surface parameters, especially on the second cone surface, show a strong dependence on the Reynolds number, with skin friction, pressure, and surface heating rates increasing and velocity slip and temperature jump values decreasing for increasing Re number. A Kelvin-Helmholtz instability arising at the shear layer results in an unsteady flow for the highest Reynolds number. These findings suggest that consideration of experimental measurement times is important when it comes to determining the steady state surface parameters even for a relatively simple double cone geometry at moderately large Reynolds numbers. *Published by AIP Publishing.* https://doi.org/10.1063/1.5022598

I. INTRODUCTION

The interaction of a hypersonic boundary layer with shock waves can lead to the laminar-turbulent transition, which, in turn, causes a substantial increase in localized aerothermal loads. The prediction of the transition process for hypersonic laminar boundary layer shock-wave interactions [shock wave boundary layer interactions (SWBLIs)] characterized by spatial regions with both sub- and supersonic flows in various degrees of thermochemical non-equilibrium and length scales is therefore key to the design of efficient hypersonic vehicles to avoid overly conservative use of thermal protection with its performance penalization. Starting with the classic experimental and theoretical work of Chapman *et al.* on supersonic shock wave boundary layer interactions (SWBLIs) with distinct separation zones,[1] there have been extensive experimental studies of flows over a flat plate, double cone and wedge, hollow cylinder/flare, and biconic configurations,[2,3] as well as modeling and simulation studies.[4–7] However, such unsteady flows can be difficult to characterize in ground based experiments primarily due to finite measurement times as well as the lack of a well-established metric to relate the establishment time of short-duration facilities with the time convergence of computations for separated flows.[8] Gaitonde *et al.*[9] found that the required time for their Navier-Stokes (NS) solution to converge was approximately 100 characteristic flow times, the latter defined as the time required to travel the length of the model at the freestream velocity. Since this estimation did not take into account the effects of the separation region and boundary layer, it is not clear that experiments performed with this sole criterium represent steady state results for a laminar flow that has not transitioned. Finally, as has been pointed out by Druguet *et al.*,[10] predicting the time evolution of SWBLIs with NS/CFD (Computational Fluid Dynamics) simulations using explicit time integration methods is difficult due to the large number of time steps required, and although an implicit time integration was adopted the time evolution of the flow was not shown. On the other hand, because the direct simulation Monte Carlo (DSMC)[11] method is time-accurate and its time step is based on the local collision frequency, and not numerical stability, it is well suited for capturing the transient behavior of unsteady flows toward transition.

The theoretical underpinning of the unsteady behavior of hypersonic SWBLIs is discussed in a number of seminal studies. Edney[12] classified six different shock interactions according to experimental observations on oblique and bow shock waves over blunt bodies. With respect to hypersonic flows over a double cone geometry, Babinsky and Harvey[13] showed that the existence of an underexpanded jet in the interaction region can be categorized as an Edney type IV pattern which exhibits inherent instabilities due to the high-frequency unsteady movements of the jet.[14] Ben-Dor *et al.*[15] studied the hysteresis effect occurring due to shock-shock interactions of inviscid hypersonic flows over a double wedge and found that either a regular or a Mach reflection that forms a Mach stem

a)Electronic mail: tumuklu2@illinois.edu.
b)Electronic mail: deblevin@illinois.edu.
c)Also at: Univeridade Federal Fluminense, Niterói, Rio de Janeiro, Brazil. Electronic mail: v.theofilis@liverpool.ac.uk.

occurs depending on the interaction angle between two shock waves. The transition phenomena between the two reflections can result from the motion of the triple point and the orientation of the shock waves, which in turn results in oscillations on the surface pressure values and shock location. Moreover, the interactions between a shock wave and acoustic or non-acoustic (entropy and vorticity) disturbance waves is another possible source for creating shock wave unsteadiness. Duck *et al.*[16] showed that the pressure disturbances along the surface of a geometry can be attributed to a wide range of wavelengths caused by the interaction between the shock wave and monochromatic disturbances. Furthermore, the interaction of these disturbance waves and monochromatic disturbances with second and higher modes as well as Tollmien-Schlichting (TS) waves in the hypersonic boundary layer are an active mechanism for transition. In particular, acoustic and entropy or vorticity waves may excite the stable mode F, which can excite the unstable mode S causing unsteadiness.[17]

Despite the extensive efforts of the hypersonic community to understand the time evolution of hypersonic laminar SWBLIs, a number of important challenges still remain. These include (1) understanding the role of three-dimensional pressure relief effects in stabilizing the recirculation region and its dependence on the Reynolds number, (2) the time evolution on the separation region and its effect on overall flow structure and surface properties such as heat flux, and (3) the role of non-continuum effects such as velocity and temperature slip at the leading edge on asymptotic time behavior of shock wave disturbances. With respect to the first item, Rudy *et al.*[4] showed that three-dimensional effects become important especially for a sharp wedge with span comparable to the separation zone size for a Mach number of approximately 14 and a Reynolds number of 240 000. Our earlier DSMC simulations of flow over a double wedge using two and three-dimensional models showed that the evolution of the separation zone has a significant effect on the overall flow structure and surface parameters, as well as the required time to achieve a steady-state solution.[18] Recent modeling and experiments[19] showed that the impact of the slip velocity has a significant impact on the size of the separation region by comparing Navier-Stokes (NS) and DSMC solutions for a "tick" configuration in the near-continuum regime. The separation size predicted by NS was found to be larger than DSMC due to the zero slip assumption.

These examples of previous work suggest that multiple length scales exist in hypersonic laminar SWBLIs and are an important ingredient of these complex flows. The inherently time accurate DSMC approach is well suited to model all length scales, especially with regard to gas-surface interaction, since velocity slip is a natural outcome of DSMC simulations and a velocity-slip approximation does not have to be made, as opposed to CFD approaches. *The objective of this paper is to use a non-continuum kinetic approach, DSMC, combined for the first time with modern global modal linear stability analysis to address the second item*. Although molecular-based DSMC provides a high fidelity baseline flow, global stability theory is required to analyze potential instability mechanisms and to determine the effect of Knudsen number and vibrational modes on the long time scale (order of 10-100 ms) stability behavior. Building on our earlier work of modeling SWBLIs for a non-reacting, axisymmetric nitrogen flow over a double-cone configuration,[20] we analyze here the change in the separation region size and the thickness of the shock and contact layers as a function of Reynolds number using the linear stability theory of Theofilis.[21–23]

The DSMC method has also been used to model SWBLIs and other time varying flows, but to a much lesser extent than CFD. Using DSMC, Moss *et al.*[24,25] demonstrated the sensitivity of surface heat flux, skin friction, and size of the separation region to key DSMC numerical parameters and used slip velocity as a numerical convergence criterion of DSMC parameters for the same double cone geometry that will be used in this paper. Moss and Bird[25] showed that the DSMC method is capable of predicting separated flow properties in the near-continuum regime accurately if all of the DSMC numerical parameter requirements, such as time step, cell size, and the total number of particles, are satisfied and obtained excellent agreement with heat flux measurements of flow over a double cone.[2,26] The hysteresis effect of flow over a wedge configuration was studied by Ivanov *et al.*[27] using DSMC and Euler/CFD approaches to investigate the importance of rarefied effects and physical viscosity. In addition to its application to SWBLIs, the DSMC method was employed to analyze flow instability.[28–30] Manela and Zhang[28] studied the temporal stability of Kolmogorov flows in the near-continuum regime with a continuum approach with velocity slip and temperature jump corrections and found that fluid compressibility has a stabilizing effect due to viscous dissipation. The second work[29] established the limits of the slip and collisionless flow assumptions by studying the flow characteristics of a one-dimensional wall bounded sinusoidal heating problem using a low-variance DSMC approach. Additionally, Manela and Frankel[30] studied the onset of convection in a Rayleigh-Benard flow with a linear temporal stability analysis and assessed the effects of compressibility, and velocity-slip and temperature jump at the walls by means of the DSMC method. Finally, Gallis *et al.*[31] investigated Rayleigh-Tayler instability using DSMC and obtained good agreement with theoretical and empirical models as well as experiments that they attributed to the ability of DSMC to accurately model viscosity, compressibility, thermal conductivity, and diffusivity.

The current work demonstrates a combination of DSMC-based simulations and linear stability analysis. Until this work, it would be fair to say, that there was *no connection* between the kinetic simulations of gas dynamics (i.e., DSMC) and modern linear stability theory. In particular, the shock-dominated hypersonic flows over the sharp 25°/55° double cone model used in the CUBRC LENS-I wind tunnel[2,26] are investigated to understand the impact that the extensive separation regions have on the temporal steadiness of the flow and the required time for it to reach the steady state for different Reynolds number cases. The outline of the remainder paper is as follows. Section II describes the models employed in the DSMC method, the selection of numerical parameters, and the modification of the sampling procedure used to model unsteady near-continuum flows. The effect of Reynolds numbers on the shock structure and surface parameters for flow solutions close to steady state are presented in Sec. III. Finally, Sec. IV

discusses the time evolution of the complex Edney type IV flow field structures and their impact on surface parameters such as heat flux. Demonstration of steady state, where it is found to occur, for different Reynolds number cases is demonstrated through the use of the residual algorithm of linear stability theory.

II. NUMERICAL APPROACH

The DSMC method of Bird[11] is a well-known stochastic approach to solving the Boltzmann equation of transport given as

$$\frac{\partial}{\partial t}(nf(c_i)) + c_j\frac{\partial}{\partial x_j}(nf(c_i)) + \frac{\partial}{\partial c_j}(F_j\, nf(c_i)) = \left[\frac{\partial(nf(c_i))}{\partial t}\right]_{\text{collision}}, \quad (1)$$

where $f(c_i)$ and n are the distribution function of class c_i and number density, respectively,[32] and the external force field acting on gas molecules, F_i, is assumed to be zero in the current work. The Boltzmann equation is the most general formulation of binary gas flows allowing for rarefaction effects such as velocity slip and temperature jump that occurs at cone surfaces, thermal nonequilibrium, and molecular nature of the flow and its effect on viscosity and thermal conduction, regardless of the flow Knudsen number. These factors influence laminar SWBLIs at the multi-scale, making the DSMC method a good candidate as a computational tool, as long as the well-known numerical criteria can be met. The Statistical Modeling In Low-density Environment (SMILE)[33] computational solver was used in all axisymmetric simulations presented in this work. SMILE employs the majorant frequency scheme[34] for modeling the right-hand side of Eq. (1), which provides a higher fidelity of the local collision frequency with fewer computational particles than the no-time counter method of Bird. The variable hard sphere (VHS) model for modeling collisions between particles[11] was used. In the VHS model, the total collision cross section is given as

$$\sigma_T = \sigma_{ref}\left(\frac{T_{ref}}{T}\right)^{\alpha}, \quad (2)$$

where σ_{ref} is the reference value of the cross section at the reference temperature T_{ref} and α is the inverse power law exponent related to the exponent w in the viscocity-temperature dependence as $\alpha = w - 0.5$. For N_2, the only gas considered, $T_{ref} = 273$ K, $\alpha = 0.24$, and the collision diameter, $d = 4.17 \times 10^{-10}$ m, where $\sigma_T = \pi d^2$ values were used. The Larsen-Borgnakke (LB)[35] model was used to model rotational-translational (R-T) and vibrational-translational (V-T) energy transfer. More specifically, Millikan and White (MW)[36] and Parker's rates[37] with DSMC correction factors[38,39] were used to model (V-T) and (R-T) relaxation rates, respectively. Finally, the gas-surface interactions were modeled using the Maxwell model with full momentum and energy accommodation.

Since the target problem is in the continuum regime for most of the domain, the numerical parameters for the DSMC simulations were carefully checked to ensure that the presented results are independent of any numerical parameters. The conventional DSMC numerical requirements are that the number of computational particles per volume with a linear size equal to the local gas mean free path, λ, be on the order of four, the time step is such that simulated particles do not cross more than one collision cell during a single time step, and the collision cell size should be less than the local mean free path. To efficiently satisfy the DSMC cell size requirement, the SMILE code employs a two-level Cartesian grid, namely, at the coarse and refined levels, to capture large flow gradients in the simulation domain. The refined collision grid is constructed by subdividing background cells based on local density gradient values, the number of particles in the cell, and a user-defined parameter which controls the maximum number of subdivisions for a given background cell. This grid adaptation algorithm guarantees that there are at least 5-6 particles for the non-reacting case per collision cell before allowing further divisions. This number of particles per collision cell is sufficient since the majorant collision frequency algorithm[34] is used while selecting the collision pairs in this work. In addition, it should also be noted that local collision frequency is calculated based on the collision cell. The coarser grid is known as the background grid, in which the sampling process to calculate macroparameters takes place. The DSMC numerical parameters used for the four different Re number cases are summarized in Table I in terms of the total number of particles, collision cells and time steps in the simulation domain.

The selection of DSMC numerical parameters involves a certain amount of trial and error because the simulations presented in this work are complicated by the large variation in length scales as well as the unsteadiness of the flow. Table II

TABLE I. DSMC numerical parameters for the axisymmetric simulations.[a]

Numerical parameters[b] for cases:	X Re	2X Re	3X Re	4X Re
Number of simulated particles	10.94×10^9	3.63×10^9	4.14×10^9	2.74×10^9
Total number of time steps	125 000	400 000	880 000	2 000 000
Time step, dt (s)	2.0×10^{-8}	8.0×10^{-9}	6.0×10^{-9}	5.0×10^{-9}
Total number of collision cells	4.51×10^8	4.70×10^8	5.270×10^8	3.70×10^8
FNUM[c]	2.5×10^7	1.5×10^8	2.0×10^8	4.0×10^8
Total computation hours[d] (CPU hours)	91 995	115 200	352 000	544 000

[a]Domain size (m), [X] × [Y] = [−0.05–0.2] × [0.0–0.25].
[b]At the end of the simulation.
[c]Number of molecules in one simulated particle.
[d]ERDC topaz high performance computing system using 960 processors with an approximate parallel efficiency of 54%.

TABLE II. The DSMC numerical parameters, per time step, at critical locations for four different cases.

Cases	X Re			2X Re			3X Re			4X Re		
Locations (m)	SP	RP	BS	SP	RP	BS	SP	RP	BS	SP	RP	BS
x	0.079	0.101	0.098	0.071	0.105	0.106	0.064	0.109	0.101	0.057	0.118	0.114
y	0.037	0.055	0.756	0.033	0.062	0.098	0.03	0.068	0.083	0.027	0.081	0.113
Parameters[a]												
λ/dx	20.13	2.27	18.70	6.68	3.31	17.34	3.69	2.54	10.27	2.76	2.26	7.49
MCT/dt	2.7	1.36	5.81	5.12	1.77	11.86	3.85	1.874	38.9	3.35	1.82	9.19
NPICC	96.052	239.4	35.661	6.014	14.43	5.68	6.85	14.45	7.62	5.62	7.94	5.14
NPIBC	152 916	384 176	57 188	38 539	92 609	12 625	52 417	92 740	5726	33 058	50 910	11 834

[a]SP = separation point, RP = reattachment point, and BS is at a point along the bow shock. Also, NPICC and NPIBC = number of particles per collision and background cell, respectively.

presents the values of the numerical parameters achieved during the simulations at three critical locations, namely, at the separation and reattachment points and a point along the bow shock, using the numerical parameters given in Table I. It can be seen that the cell sizes, dx, are sufficiently small such that the local mean free path to collision cell size ratio (λ/dx) is larger than 2 throughout the domain and for all Reynolds number cases. It can also be seen that the time steps used for the different cases (see Table I) allowed the ratio of the mean collision time to the time step (MCT/dt) to be greater than unity. With respect to the number of particles per collision and background cells, it can be seen that there is a large difference between the X Re values and the other three cases. Moss and Bird[25] simulated the X Re number case using about 16×10^6 particles, whereas in our work it was increased by a factor of about 700 to ensure that there would be a sufficient number of particles in background cells to accomplish macroparameter sampling with sufficient statistics. Unlike this work, however, the results of Moss and Bird[25] are presented only at steady state. Furthermore, although the DSMC is a time accurate algorithm, sampling of the flowfield macroparameters to obtain their steady state values does not usually occur until the flow formation or transient period is completed. However, in the simulations presented in this work, the sampling process was modified such that the macroparameters at selected critical locations were sampled during *each* time step in order to accurately capture the time evolution. Therefore, to achieve sufficient statistics, much higher numbers of particles per collision and background cells than is typical were employed generating $\sim 11 \times 10^9$ computational particles in the domain (see Table I). This is certainly a large computational load for the *lowest* Re number which would be very difficult to sustain when scaled up to the higher Re number cases. Since a comparison of the DSMC solutions presented here with 11×10^9 particles was found to be essentially the same as an earlier simulation that employed about 2.5×10^9 particles,[40] smaller, but, correct numbers of computational particles were used in the higher Reynolds number cases, as shown in Table II. It should be noted that contour plot and surface parameters shown in this paper for a given time represent an average over the NPIBC values given in Table II for 500 time step samples collected before and after the indicated time, unless stated otherwise. This sample size is large enough to reduce the statistical noise and small enough to capture unsteadiness since a sufficiently small time step is used for all cases.

III. VARIATION OF FLOW STRUCTURE AND SURFACE QUANTITIES WITH REYNOLDS NUMBER

A. Effect of Reynolds number on SWLIs

In previous work,[20] a hypersonic flow over a double-cone geometry was studied for flow conditions of a nitrogen gas with a freestream vibrational temperature of 1986 K and translational and rotational temperatures equilibrated to 42.6 K. The elevated vibrational temperature in the freestream is a general outcome of the reflected shock tunnel facilities since the test gas is compressed and heated by a reflected shock and a rapid expansion through the nozzle results in high vibrational temperature associated with a lower vibration relaxation rate in comparison to translational and rotational relaxation rates. The stagnation enthalpy of 2.2 MJ/kg is low enough to ensure that the flow is chemically frozen[13] so that no chemical reactions including N_2 dissociation were modeled. The current work focuses on the impact of Reynolds numbers on the flow structure and the required time to achieve steady state by changing the freestream Re number while keeping the geometry and freestream conditions of $M_\infty = 15.88$, $T_{trn} = T_{rot} = 42.6$ K, $T_{vib} = 1986$, $U_\infty = 2073$ m/s, and a stagnation enthalpy of 2.2 MJ/kg the same. The static pressure for the X Re case of 2.2 Pa was increased to 8.8 Pa for the 4X Re case giving a change in the freestream Reynolds number of 9.35×10^4 (X Re)–3.74×10^5 m^{-1} (4X Re).

Figure 1 shows the variation of the complex Edney Type-IV shock wave flow structure captured through the computed Schlieren contours of the density gradient. The overall shock structure for different Re number cases is similar and shows the attached shock originating from the leading edge of the first cone interacting with the detached shock formed by the second cone. The interaction of these shocks forms the triple point (T), a shear layer passing through M, and a transmitted shock which impinges on the reattachment point (R), resulting in localized heat and pressure loads. This outer shock structure is further modified by the separation zone and the boundary and shear layers. As can be seen from the DSMC simulations, the supersonic flow bounded by the points T, M, and R shown in Fig. 1(c) is compressed by a high-pressure subsonic flow due to the strong bow and transmitted shocks, resulting in an underexpanded flow confined by two contact surfaces, C1 and C2. C1 is formed between the subsonic hot stream and the cold supersonic jet, whereas C2 is formed between the boundary layer and the supersonic cold jet.[13] The underexpanded flow

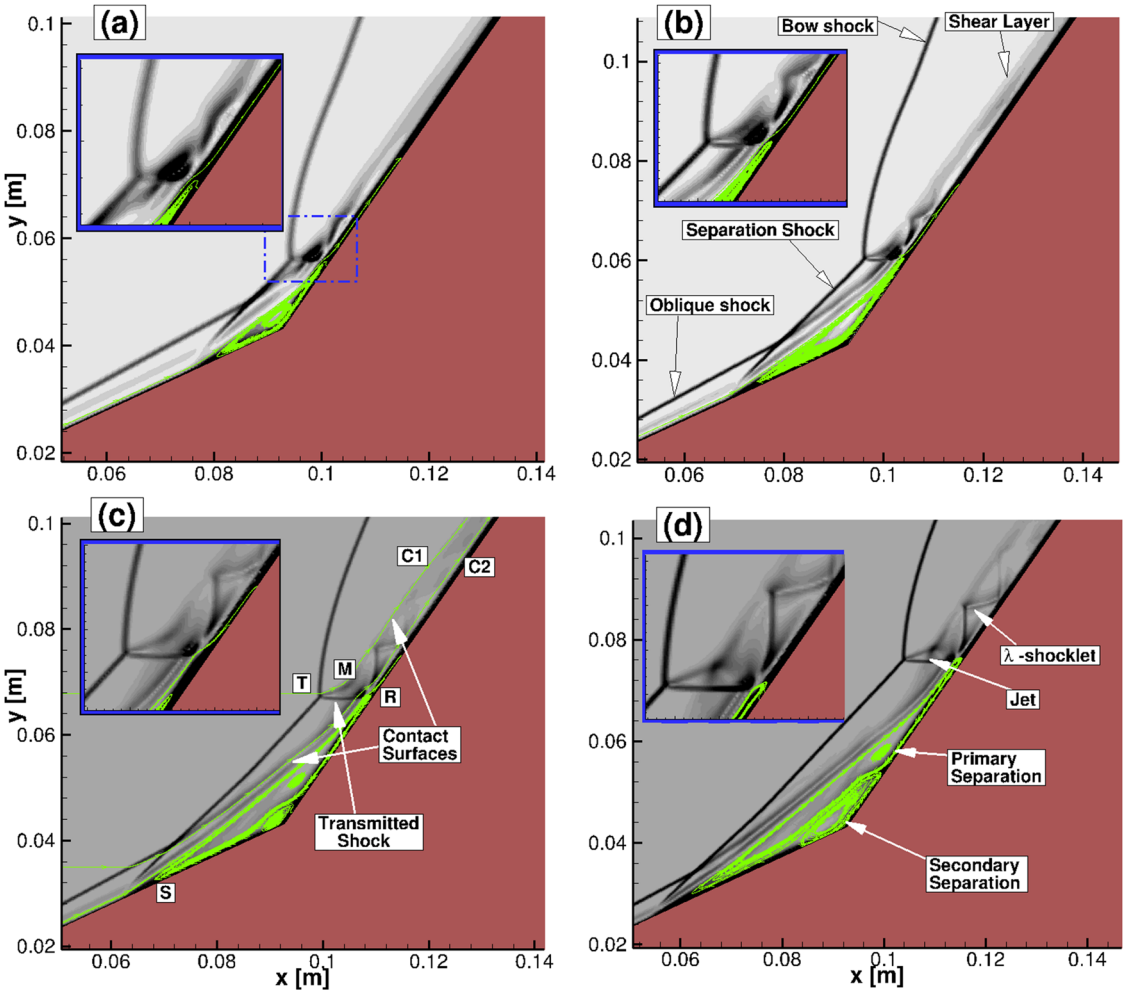

FIG. 1. Variation of the SWBLI with respect to Reynolds numbers, (a) X Re, (b) 2X Re, (c) 3X Re, (d) 4X Re cases, based on computed Schlieren with distinct features of S: Separation point T: Triple point, R: Reattachment point.

passes between C1 and C2 with a series of the compression and expansion waves in the shape of a λ shock let to direct the jet through the cone surface.

Consistent with oblique-shock theory, the shock angle for all Re number cases is calculated as about 28.3° based on the alignment of the fitted line shown in Fig. 2(a) denoted as A-B. According to Taylor-Maccoll theory for conical flows, which assumes that the length of a cone is infinite,[41] the shock angle was calculated as 27.3° based on the first cone angle of 25°, a specific heat ratio of 1.34, and a freestream Mach number of 15.88. The one-degree difference can be attributed to viscous effects since the finite length of the cone does not have an effect on the shock angle. As will be discussed, the existence of the second cone does not influence the flow field and surface parameters of the first cone prior to the separation region. Similarly, the separation shock angle (angle between a line parallel to the x axis and dotted line C-D) is measured as 45.27°, 44.98°, 46.40°, and 46.41° for X, 2X, 3X, and 4X Re cases, respectively, suggesting that under these circumstances, the separation shock angle does not change significantly with Reynolds number as well. It should be noted that due to the uncertainty in the shock thickness for the lower (X and 2X) Re cases and the short separation shock extent shown as C-D in Fig. 2(b), the lower Re cases may not be a good candidate for the estimation of the separation shock angle. The interaction between the oblique and bow shocks decreases the downstream pressure which in turn changes the alignment of the separation shock. This is obvious especially for the higher Re cases, as can be seen in Figs. 2(b) and 2(c).

As Fig. 1 shows, however, increasing the Re number alters the distinct flow features of the SWBLI such as the size of the separation region, the thickness of the shock, and the distance between the contact layers. Specifically, a larger separation region and thinner shocks are formed for the higher Re cases. The length of the separation region, i.e., the distance between the separation and reattachment points presented in Table II, is calculated as 0.028, 0.045, 0.059, and 0082 m for the X, 2X, 3X, and 4X Re cases, respectively. The larger distance between C1 and C2 and greater pressure values in the TMR region in the higher Re number cases makes the λ-shocklets more distinctive. The pressure contours and formation of the separation shock for the different Reynolds-number cases is shown in Fig. 2. A large adverse pressure gradient forms compression waves in the vicinity of the separation region, and these waves eventually coalesce and form the separation shock. The boundary layer thickness determines the extent of these

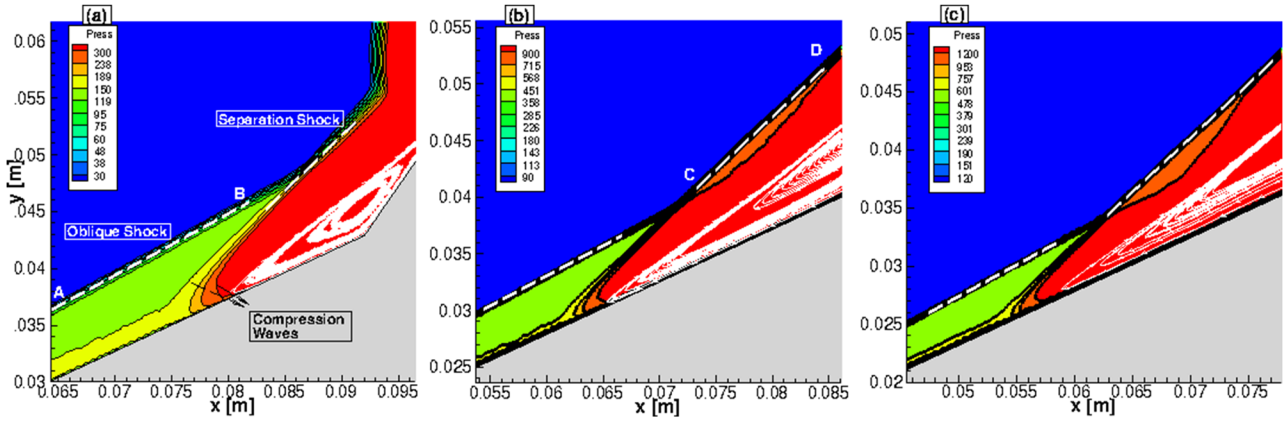

FIG. 2. Spatial distribution of pressure in the vicinity of the separation point for the (a) X Re case, (b) 3X Re case, (c) 4X Re case.

waves, and therefore the extension of the compression waves is small for the highest Re number case due to the thinner boundary layer.

Furthermore, increasing Reynolds number yields a secondary vortex structure in the separation zone, as can be seen in Figs. 1(c) and 1(d). The change in the topology of the separation zone in fact suggests that as the Reynolds number is increased the flow becomes more unstable. Reference 21 studied the instability properties of incompressible laminar boundary layer flows over a two-dimensional flat-plate and found that the regime with the multiple bubbles originating from the merging of separation and reattachment points is structurally unstable to three-dimensional perturbations. This instability scenario has also been confirmed to exist in a multitude of massively separated flows (see Ref. 42 for details). As will be shown in Sec. IV, the time characterization of the unsteady flow involves the interaction of the strong shock features with the recirculating region and the interaction of the different flowfield features will vary for different Reynolds numbers.

B. Variation of flows macroparameters with respect to Reynolds number

The base flow macroparameters for the 2X Reynolds number case are shown in Fig. 3. Consistent with the relatively fast translational-rotational relaxation rates and the flow Mach number, the translational temperatures shown in Fig. 3(a) and rotational temperatures (not shown) are found to be much closer to each other, whereas the vibrational temperature is frozen in most of the region downstream of the shock except in the boundary layer and the separation region. It should be noted that the effect of N_2 molecular emission is negligible due to the low translational temperature with a maximum value of about 2100 K. As shown in Fig. 3(b), the vibrational temperatures decrease downstream of the shock region especially in the vicinity of the boundary layer and separation region due to collisions with the fully thermal accommodated diffusive cold wall at a constant temperature of 297.2 K. With respect to the other Reynolds number cases, it was observed that in the highest Re number case, due to a larger separation zone, the vibrational temperatures were found to be somewhat lower due to the faster translational-rotational relaxation associated with the higher density.

Earlier simulations of unsteady flows over a double wedge for argon, air, and nitrogen gases showed that the relative magnitude of the ratio of specific heats plays a critical role in SWBLIs. In particular, the size of the separation region for an argon flow over a double wedge at Mach 7 was found to be larger by a factor of 1.8 than that for nitrogen. Similarly, due to endothermic chemical reactions for a reacting air case, the separation region shrinks by a factor of 1.5 in comparison to

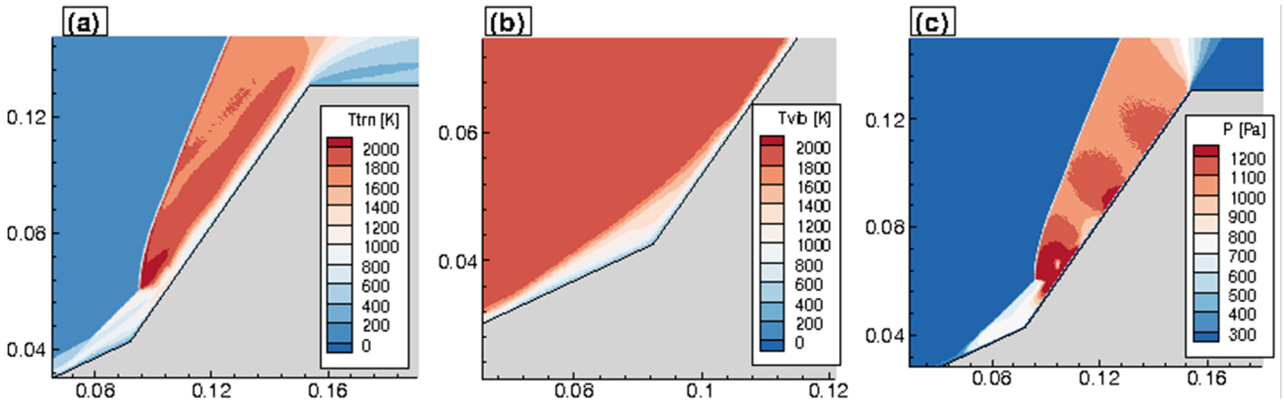

FIG. 3. Spatial distributions of base flows for the 2X Reynolds number case, (a) translational temperature, (b) vibrational temperature, and (c) pressure.

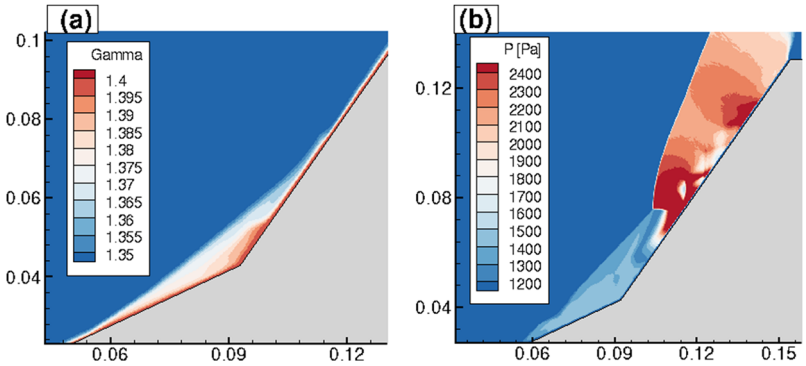

FIG. 4. Spatial distributions of flowfield parameters for the highest Re number: (a) specific heat ratio, (b) pressure.

the non-reacting nitrogen case.[43] For the double cone study of this work, the local specific heat ratio distribution also shows an increase near the surface due to the fact that the contribution of the vibrational degree of the freedom decreases as can be seen in Fig. 4(a). The specific heat ratio was calculated from standard kinetic theory as

$$\gamma = \frac{\xi_{trn} + \xi_{rot} + \xi_{vib} + 2}{\xi_{trn} + \xi_{rot} + \xi_{vib}}, \tag{3}$$

where the translational, ξ_{trn}, and rotational, ξ_{rot}, degrees of freedoms are 3 and 2 for molecular nitrogen, respectively, and a simple harmonic oscillator model for the vibrational mode is used to calculate the effective number of vibrational degrees of freedom given as

$$\xi_{vib} = \frac{2\theta_v/T_{vib}}{\exp(\theta_v/T_{vib}) - 1}, \tag{4}$$

where the characteristic temperature, θ_v, is 3371 K for nitrogen.

Pressure fluctuations on the second cone resulting from expansion and compression waves that occur in between the two sonic lines, C1 and C2, can be observed in Figs. 3(c) and 4(b). Note that Ref. 5 also observed similar structures for inviscid shock wave interactions of flows over a double wedge geometry. At the higher Reynolds number case, Fig. 4(b) shows that compared to Fig. 3(c) there are fewer repetitions of the increasing-decreasing pressure patterns. This reduction in the pressure variation pattern occurs because the triple point moves downstream and the length of the second cone surface is not long enough to observe the alternating minima and maxima trend in pressure values.

The DSMC method provides the ability to study the kinetic nature of the flow non-equilibrium due to strong gradients in the shock interaction region through collection of the particle velocity distribution functions. The four locations across the bow shock that were selected are shown in Fig. 5(a) for the lowest Re number case. In order to reduce the statistical noise in the probability distribution functions, velocity values for about 3.2×10^6 particles averaged over 23 time steps at steady state were used at location 6 (near the separation point). As shown in Fig. 5(b), at the onset of the shock, location *a*, two distinct peaks at 0 and 2073 m/s corresponding to particles that have collided downstream of the very narrow shock region and those that have come from the free-stream and not undergone any collisions, respectively, can be seen. This classic bimodal distribution continues further downstream, points *b* through *c*,

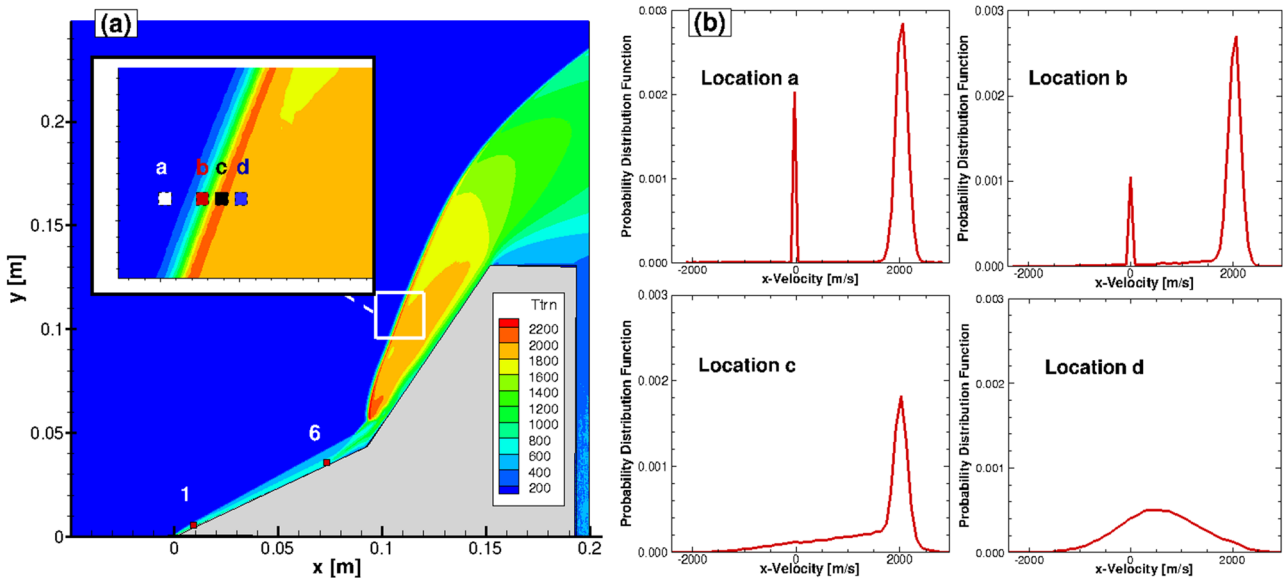

FIG. 5. (a) Translational temperature counters and locations for data probing; (b) x-velocity distribution in bow shock for the lowest Re case at 2.4 ms.

with the population of particles from the first class continuing to increase and the freestream particles decreasing. Finally, a hot stream of particles form a Maxwellian distribution further downstream at location d as the velocity distribution of particles normal to the streamwise direction broadens.

At locations 1 and 6 in the vicinity of the leading edge and separation point, respectively [see Fig. 5(a)], the particle distribution functions are compared to Maxwellians based on the local translational temperature in Figs. 6(a) and 6(b), respectively, at 2.4 ms. At location 1, although some differences are present due to rarefaction effects, good agreement between the velocity distribution function obtained from DSMC and a Maxwellian fit is achieved. At locations further downstream, this agreement improves. The time variation of the distribution functions is found to be small, but the drop in gas temperature as the flow reaches steady state can be observed from the DSMC velocity distributions directly. For example, at location 6, at an earlier time of 0.8 ms, the translational temperature and average velocity obtained from the x-velocity values were found to be 685 K and 113.3 m/s with standard deviation values of 0.51 and 0.795, respectively. The Maxwellian shown in Fig. 6(b) at 2.4 ms has an average temperature and velocity of 668 K and 91 m/s, respectively, showing that the flow is cooling and the average velocity decreases by about 19%. Moreover, the theoretical Maxwellian distribution based on the local flowfield values for all Reynolds number cases agrees well with the distribution based on particles data even where the λ-shocklet structure occurs for the highest Re number case [see Fig. 1(d)]. These suggest that the role of viscosity is sufficiently small at these conditions such that the use of the ES-BGK model, an approximation to the Boltzmann equation based on the linearization of the collision integral,[20] would be correct.

C. Surface parameters

Comparison of modeled and measured surface parameters provides an important tool in studying SWBLIs. Therefore, understanding their variation with the Re number and temporal evolution of these quantities provides clues about the interaction of the shock layer with the recirculation region. First, Fig. 7 shows the Re number variation of skin friction and heat transfer rates and velocity slip. Consistent with simple, incompressible flow Blasius boundary layer theory, the skin friction coefficient, C_f, along the first cone surface decreases with the square root of the Reynolds number, as seen in Fig. 7(a). The highest Re case exhibits a larger separation region and shows stronger fluctuations in the aft part of the cone ($0.12 < x < 0.15$ m). Figure 7(b) shows that the magnitude and peak of the surface heat transfer increases with increasing Re number because the boundary layer becomes thinner due to stronger compression.[4] The maximum in the heat flux shifts in the downstream direction as the size of the separation region increases for the higher Re number cases. These interactions, however, do not have an effect on the heat flux values along the first cone upstream of separation, as can be seen in Fig. 7(c) where they are compared for a single and double cone. This result suggests that the accuracy of the calculation along the first cone prior to the separation region can simply be tested without including the complex shock wave boundary layer interactions that result from the second cone. The inset of Fig. 7(b) also addresses the adequacy of the selected DSMC numerical parameters because DSMC predictions of surface parameters are highly sensitive to the numerical parameters of number of particles per collision cell, number of collision cells, and time step. It can be seen that for the lowest Re number case, the predicted heat flux is the same for this work and an earlier simulation with four times larger number of particles and collision cells and a smaller time step by a factor of two[40] showing that the DSMC numerical parameters of this work are numerically converged. Moreover, they both compare well with experiment,[2] especially in the separation region where heat flux values decrease.

Consistent with the decrease of Knudsen number for increasing Reynolds number, the velocity slip shown in Fig. 8(a) at the leading edge is higher for the lowest Reynolds

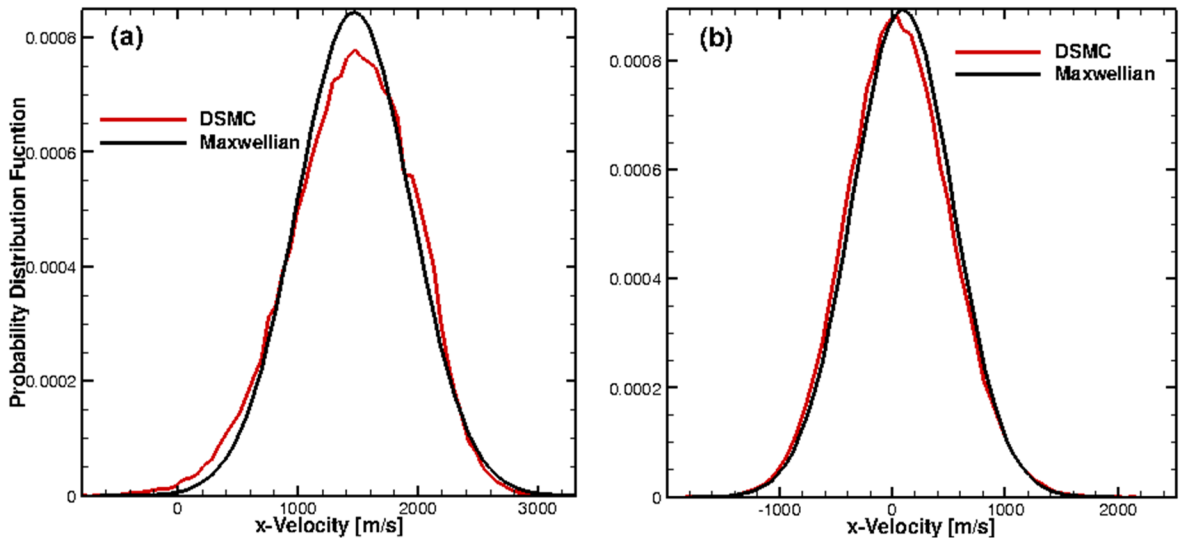

FIG. 6. x-velocity distribution for the lowest Re case at locations shown in Fig. 5 (a) at 2.4 ms: (a) location 1 or leading edge and (b) location 6.

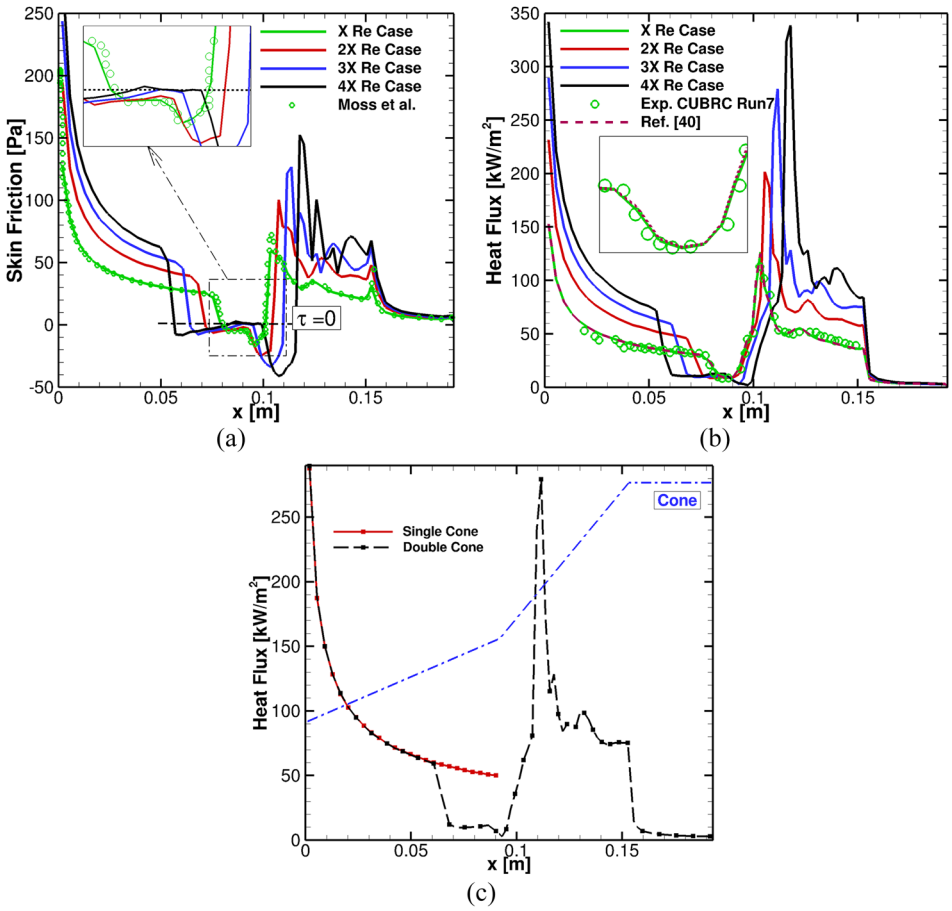

FIG. 7. Effects of Reynolds number on surface parameters and comparison with a single cone configuration. (a) Skin friction; green circle symbols correspond to the DSMC data of Moss and Bird.[25] (b) Heat flux, comparison with the experiment[2] and previous work[40] for the lowest Re case. (c) Comparison of the heat fluxes for the single and double cones for the 3X Re case at steady state.

number. The length of the separation region and the presence of a secondary vortex can be obtained by identifying the locations where the slip velocity is zero. This slip velocity profile although decreasing in magnitude with decreasing Kn number can still be seen to be relatively large at the leading edge of the first cone which has an effect on the overall flow structure. According to Gökçen *et al.*,[44] an approximate, simplified Maxwell velocity slip, V_d^M, given by

$$V_d^M = \frac{2-\sigma}{\sigma}\lambda\frac{\partial V_{\tan}}{\partial n} \tag{5}$$

can be used to calculate the velocity and temperature jump for small Knudsen number flows. In Eq. (5), σ is the momentum accommodation coefficient, assumed to be unity in the current work, λ is the local mean free path, $V_{\tan}$ is the tangential component of the gas velocity adjacent to the surface, and n is the normal direction. To test this approximation, the tangential velocity calculated from DSMC and its derivative with respect to the normal direction at the leading edge ($x = 0.04$ m) is shown in Fig. 8(b). As the Reynolds number increases, the derivative term becomes larger, whereas the local mean free path λ decreases. The effect of the latter dominates, and therefore, the velocity slip decreases with increasing Reynolds number under the given flow conditions. The percentage differences between the calculated slip values, V_d^M, and the DSMC results at $x = 0.04$ m shown in Fig. 8(a) are 17, 9.6, and 3.8 for

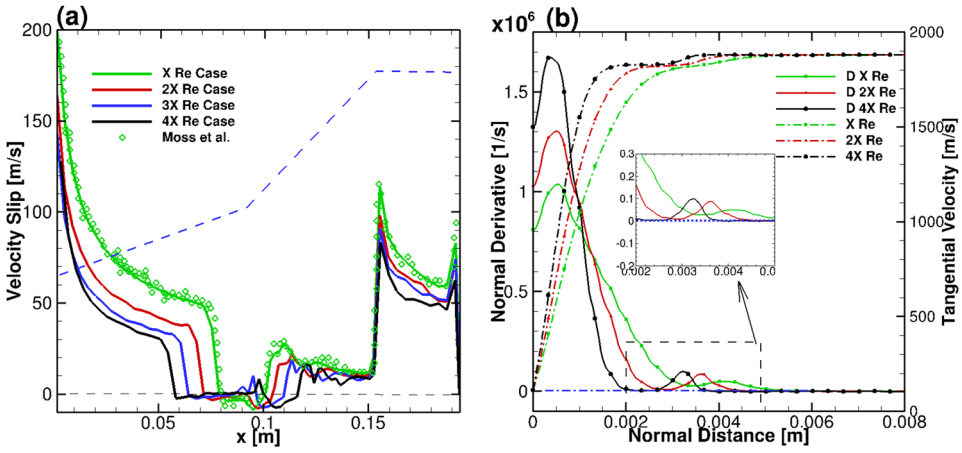

FIG. 8. Effects of Reynolds number on (a) velocity slip; (b) tangential velocity and its derivative with respect to the normal at x = 0.04 m.

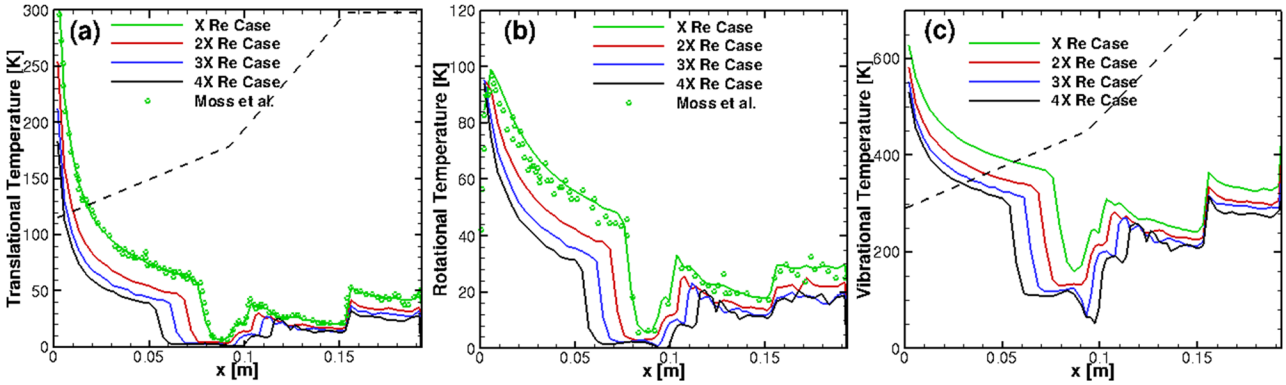

FIG. 9. Effects of Reynolds number on temperature jump calculated by taking the difference between the gas temperature at the surface and the wall temperature with a value of 297.20 K at steady state for X, 2X, and 3X Re cases and 7.5 ms for 4X Re case: (a) translational, (b) rotational, and (c) vibrational.

the X, 2X, and 4X Re cases, respectively. This suggests that Eq. (5) provides a good approximation for calculating slip for local Knudsen number smaller than 2.64×10^{-5}.

Similar to velocity slip, jump temperatures are another important feature of the DSMC simulations. The surface translational, rotational, and vibrational slip temperatures in the normal ($T_{trn,n}$), tangential ($T_{trn,\tau}$), and lateral ($T_{trn,L}$) directions are determined from the corresponding energy of incident, i, and reflected, r, particles that strike the surface element and is normalized by the normal velocity component to transform fluxal quantities,[25] i.e.,

$$T_{trn,d} = \frac{m}{k}\left[\sum_{j=1}^{N_{hit}}\left(\frac{V_{dji}^2}{|V_{nji}|}+\frac{V_{djr}^2}{|V_{njr}|}\right) \times \left(\sum_{j=1}^{N_{hit}}\left(\frac{1}{|V_{nji}|}+\frac{1}{|V_{njr}|}\right)\right)^{-1} - V_d^2\right], \quad (6)$$

where the subscript d stands for the n, τ, L directions and V_d is the velocity slip at each of the corresponding directions, i.e.,

$$V_d = \left[\sum_{j=1}^{N_{hit}}\left(\frac{V_{dji}}{|V_{nji}|}+\frac{V_{djr}}{|V_{njr}|}\right)\right] \cdot \left[\sum_{j=1}^{N_{hit}}\left(\frac{1}{|V_{nji}|}+\frac{1}{|V_{njr}|}\right)\right]^{-1}. \quad (7)$$

The translational temperature jump is calculated by subtracting the wall temperature from the temperature value obtained by averaging over the surface temperatures in the aforementioned directions. In a similar fashion, the averaged surface rotational and vibrational energy can be calculated as

$$E_f = \left[\sum_{j=1}^{N_{hit}}\left(\frac{e_{fji}}{|V_{nji}|}+\frac{e_{fjr}}{|V_{njr}|}\right)\right] \cdot \left[\sum_{j=1}^{N_{hit}}\left(\frac{1}{|V_{nji}|}+\frac{1}{|V_{njr}|}\right)\right]^{-1}, \quad (8)$$

where e denotes the internal energy of particles striking a surface element and f represents either the rotational or vibrational mode. After obtaining the internal surface energy values, the corresponding rotational and vibrational temperatures are calculated using $T_{rot} = E_{rot}/k$ and $T_{vib} = \theta_v[\ln(k\theta_v/E_{vib}+1)]^{-1}$, respectively, where $m = 4.65 \times 10^{-26}$ kg for nitrogen.

Figure 9 shows the temperature jump values obtained from Eqs. (6)–(8). Similar to the velocity slip, the temperature jump is smallest for the highest Reynolds number case. There is a significant temperature jump decrease in the separation zone for all three modes. It should be noted that the vibrational temperature jump is about four times larger than the other modes, suggesting that the effect of the vibrational accommodation coefficient on the surface heat flux could be important due to the large value of the temperature gradient in the wall normal direction. Reference 13 reported that the agreement between heat flux measurements[26] and calculations could be improved with a partially accommodating coefficient which is the most common case for metallic surfaces. Nonetheless, Moss and Bird[25] showed that this is not the case for the current work and the results are already in good agreement in terms of heat flux values when full thermal accommodation is used. Finally, as shown in Figs. 7–9, the agreement between the SMILE code and another DSMC program called DS2V is good, showing that the simulations presented here were performed in an accurate manner and that for the X Re case there is consistency across different DSMC computational platforms.

IV. TIME CHARACTERISTICS OF FLOWS OVER A DOUBLE CONE FOR DIFFERENT REYNOLDS NUMBERS

The flow fields and surface quantities shown in Sec. III were presented for flow times corresponding to the steady state at the number of time steps given in Table I for the different Reynolds number cases. The usual way to determine whether an external DSMC flow over a body has reached steady state is to estimate the time it would take for a computational particle to traverse the domain and then multiply by a factor of two or three. As mentioned earlier, we are usually only interested in the steady state solution and to avoid averaging in the transient flow development do not initiate sampling of macroparameters until the flow has fully formed or established. In other words, the additional collisions in the time steps beyond the formation of the flow are to enable sufficient statistics in macroparameter and surface quantities. However, as Table I shows, modeling of SWBLIs generally requires much longer flow establishment times than flows over simple body shapes. Although one could continue the DSMC simulation for a series of time intervals, comparing the solutions at the end of these time periods to establish that the solution is no longer changing, this is computationally very expensive and does not provide a rigorous approach for determining steady state for these types

of transient flows. For this reason, linear stability theory has been used to analyze the time convergence of the DSMC solutions.

In the work of Theofilis,[45] it has been shown that for flow times close to convergence, any macroscopic flow parameter, $\mathbf{q} = (u, v, T_{\text{trn}}, T_{\text{rot}}, T_{\text{vib}}, P)^T$, can be represented by the linear superposition of a steady solution, $\bar{\mathbf{q}}(x, y, z)$, and a small three-dimensional deviation from the steady state, denoted as residual, $\tilde{\mathbf{q}}(x, y, z, t)$, i.e.,

$$\mathbf{q}(x, y, z, t) = \bar{\mathbf{q}}(x, y, z) + \epsilon\tilde{\mathbf{q}}(x, y, z, t), \tag{9}$$

where ϵ is assumed to be small. Three-dimensional perturbations developing from a steady laminar two-dimensional base state can be described by a perturbation of the form

$$\tilde{\mathbf{q}}(x, y, z, t) = \hat{\mathbf{q}}(x, y)\mathrm{e}^{\mathrm{i}[m\phi-\omega t]} + c.c. \tag{10}$$

where $m = 0, 1, 2, \ldots$ is an integer azimuthal wavenumber parameter. The present analysis assumes two-dimensional perturbations with stationary disturbances[40] which may not strictly be the case for high Re number flows. In particular, the formation of a secondary vortex in the separation region is susceptible to centrifugal disturbances and can cause Görtler type instabilities in the vicinity of the reattachment point,[46] resulting in three-dimensional flow characteristics. Nonetheless, the axisymmetric assumption still holds for moderately low Reynolds number flows so that Eq. (10) can be written as

$$\mathbf{q}(x, y, t) = \bar{\mathbf{q}}(x, y) + \epsilon\,\hat{\mathbf{q}}_r\mathrm{e}^{\sigma t}, \tag{11}$$

where $\hat{\mathbf{q}}_r$ is the real part of the amplitude function and σ is the damping rate of the solution. The convergence of $\mathbf{q}(x, y, z, t)$ toward $\bar{\mathbf{q}}(x, y, z)$ can be studied by examination of the time evolution of macroparameters at numerical probes placed at local points in the flow at known critical locations such as the separation and reattachment points. Moreover, the average damping rate of the least damped perturbation was obtained by analyzing the unsteady DSMC macroparameters at those probe locations.

The time evolution of the flow quantities such as velocities, temperatures, and pressure fields of the 3X Re number case and the corresponding optimal exponential curve fit of each data set at the start of the separation region is shown in Figs. 10(a)–10(c) and the associated insets. An adverse pressure gradient at the separation point causes the flow to separate which in turn increases the interaction time with the cold wall. Therefore, all temperatures are found to decrease with

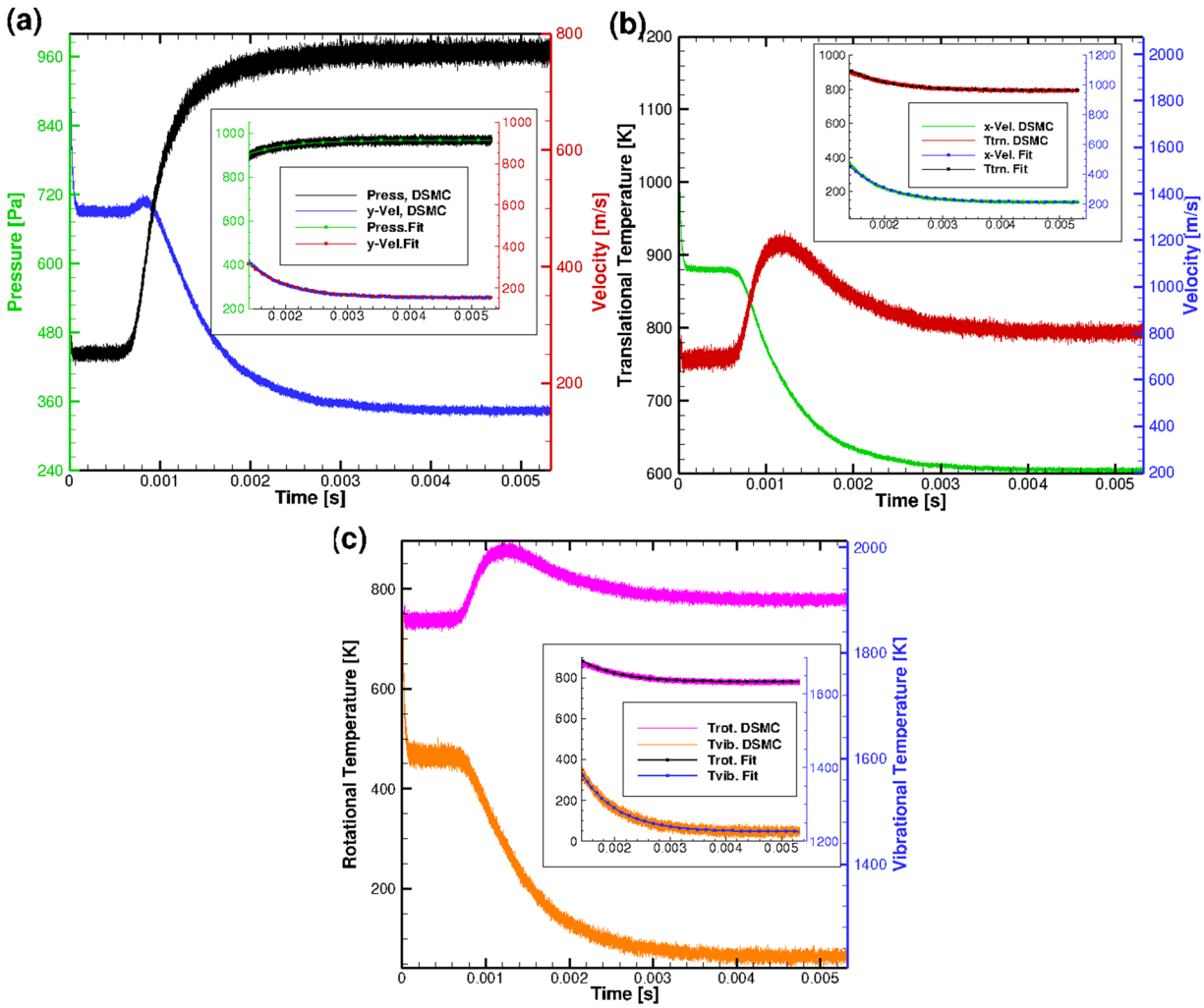

FIG. 10. Convergence history at the separation point, (x, y) = (0.066, 0.0315) (m), showing DSMC-obtained results and corresponding curve fitting: (a) pressure (Pa) and y-velocity (m/s); (b) translational temperature (K) and x-velocity (m/s); (c) rotational and vibrational temperature (K) for the 3X Re case.

time in an exponential manner. In contrast to direct numerical simulations (DNS) where the decay rate can be found by taking the derivative of the logarithm of the signal, the decay rate cannot be directly determined from the stochastic DSMC signal due to statistical fluctuations. Therefore, the time history of each macroparameter is fit to an exponential curve to obtain the value of the decay rate, σ, in Eq. (11). Consistent with the previous observation[40] where a single decay rate of $-3950\ s^{-1}$ fits the probed data at different locations for the lowest Re case, the best fit value for the decay rate, σ, for all macroparameters at the separation point and other locations was found to be $-1514\ s^{-1}$ for the 3X Re number case.

Similarly, the time evolution of the flowfield parameters in the vicinity of the separation point for the highest (4X) Re number case is shown in Fig. 11. The size of the separation region becomes significantly larger, as presented in Table II, and the separation shock becomes sharper in comparison to the lower Re number cases. As shown in Fig. 11(a), the pressure values are found to increase similar to the previous case in an exponential manner. It is interesting to note that the y-velocity values increase in time due to the formation of separation shock in this location. In comparison to the lower Reynolds number case, the boundary layer becomes thinner which is consistent with the fact that the Knudsen number is smaller and the effect of the cold wall on the temperature values is not observed. As opposed to the previous case, Figs. 11(b) and 11(c) shows that the translational and rotational temperatures increase due to the separation shock, whereas the vibrational temperature relaxes with the other modes due to the higher collision rate, in comparison to the lower Re number cases. The observations present for the 2X Re case also hold, and the decay rate was found to be $-2147\ s^{-1}$. All findings suggest that the magnitude decay rate of the least damped eigenmode decreases with Reynolds number which in turn increases the required time to reach steady state.

Time traces of pressure and the translational temperature values at three additional locations are shown in Fig. 12. As opposed to the previously shown probe data in Fig. 11, low-frequency fluctuations in both pressure and translational temperatures are observed in the boundary layer, as shown in Fig. 12(a). It should be noted that location A is closer to the

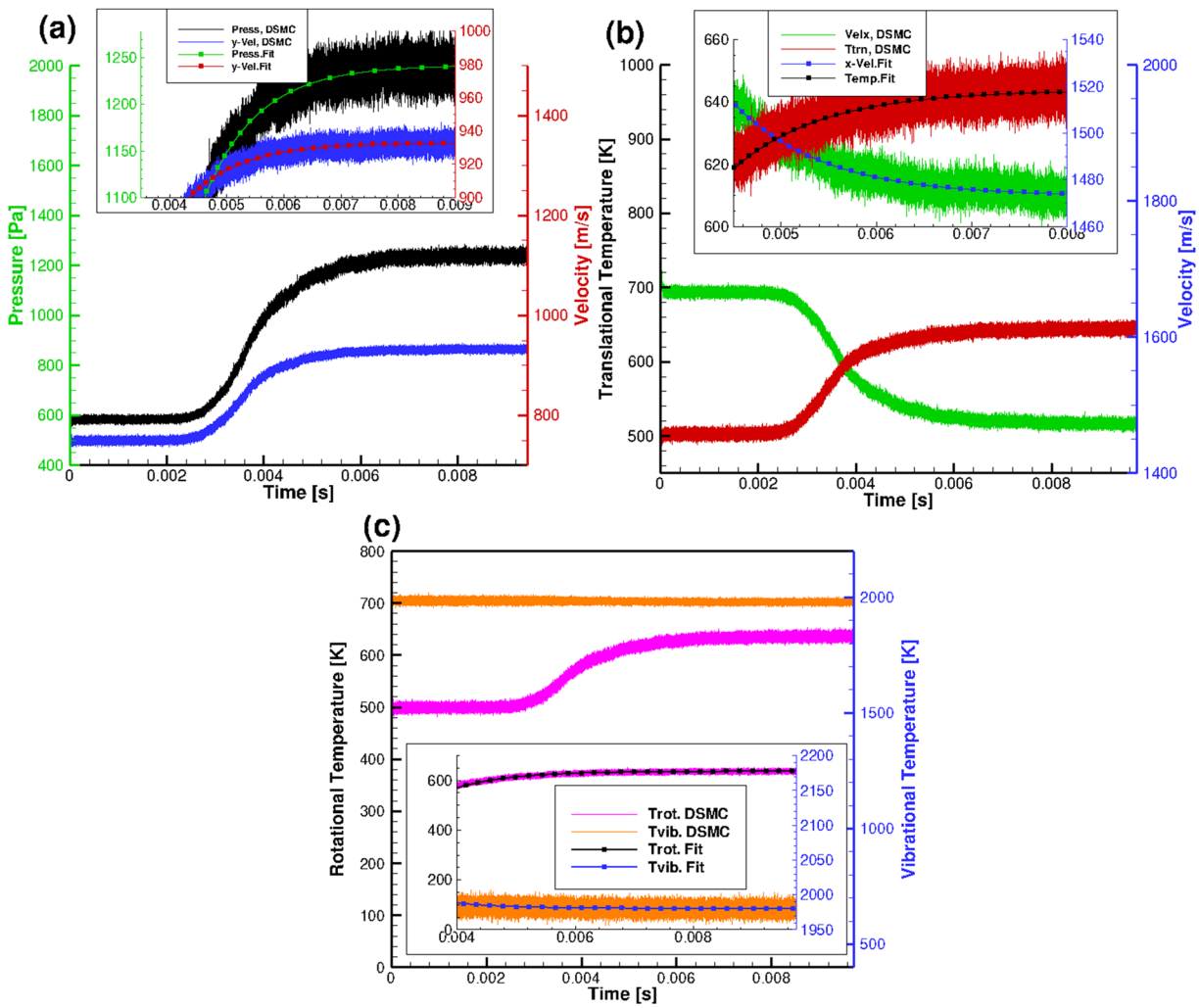

FIG. 11. Convergence history in the vicinity of the separation point at (x, y) = (0.058, 0.0294) (m), showing DSMC-obtained results and corresponding curve fitting (a) pressure (Pa) and y-velocity (m/s); (b) translational temperature (K) and x-velocity (m/s); (c) rotational and vibrational temperature (K) for the high Re case.

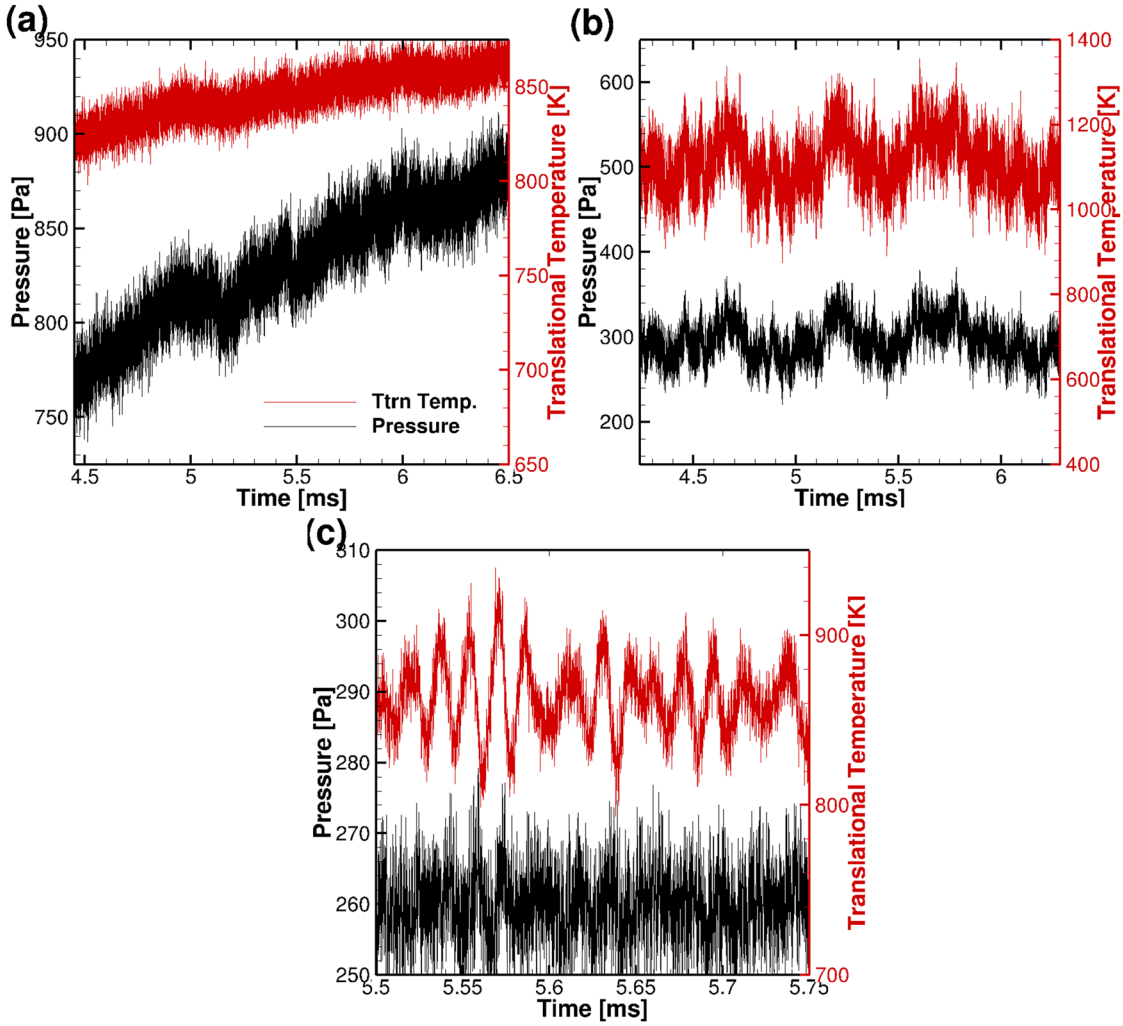

FIG. 12. Time traces of pressure and the translational temperature at (a) location A, (x, y) = (0.055, 0.027) (m); (b) location B, (x, y) = (0.113, 0.111) (m); (c) location C, (x, y) = (0.191, 0.157). Note that probe locations are shown in Fig. 13 and correspond to the separation point, a point in the bow-shock, and a location in the shear layer where a KH instability takes place, respectively.

geometry than the probe location in Fig. 11. The existence of the lower frequencies in the boundary layer suggests that the flow is not laminar.[47] Although an exponential increase dominates at the separation point, the frequency of separation shock oscillations, shown in Fig. 12(b), is somewhat similar to that of the bow shock, indicating that the separation and bow shocks are coupled to each other.

To determine the time characteristics of flowfield parameters with respect to the Reynolds number more closely, the differences between two different time solutions of the translational temperatures are shown in Fig. 13. The most striking similarities between the fields are that all features are common in the separation and bow shocks and the contact surface C1 (shown in Fig. 1) for all Re cases. This emphasizes that the magnitude of the amplitude function $\hat{\mathbf{q}}(x, y)$ is large at these locations. For the lowest Re case, the temperature in the bow shock increases in time, indicating that the bow shock moves in the upstream direction. As opposed to this trend, the shock moves in the downstream direction for the higher (3X and 4X) Re cases based on the sign of the temperature difference as can be seen in Figs. 13(b) and 13(c). This difference is more likely due to the relative position of the triple point relative to the cone. Additionally, the temperature variations in the vicinity of the regions where the λ-shocklets are located, in the location of the secondary vortex and along C1 [see Fig. 1(c)], become more significant when the Reynolds number increases. Inspecting Fig. 13(d) for the highest Re case, it can be seen that the differences in temperature along C1 are large compared to the lower Re number cases. For instance, when Re is increased, one can observe an emerging Kelvin-Helmholtz (KH) instability along the edge of the second cone arising at the shear layer. As shown in Fig. 12(c), the most dominant frequency of the KH instability is about 20 times larger than that of the bow shock oscillations. Moreover, it was also observed that the flow does not reach steady state even though the simulation was run two times further in time in comparison to the 3X Re case. Even though the flow did not reach steady state, however, the previously shown heat flux values for the 10.5 and 11 ms times are essentially the same which can be attributed to the large distance between C1 and the cone surface and the small temperature difference as shown in Fig. 13(d).

The pressure differences in the bow shock shown in Fig. 14 exhibit similar characteristics to the temperature field. The

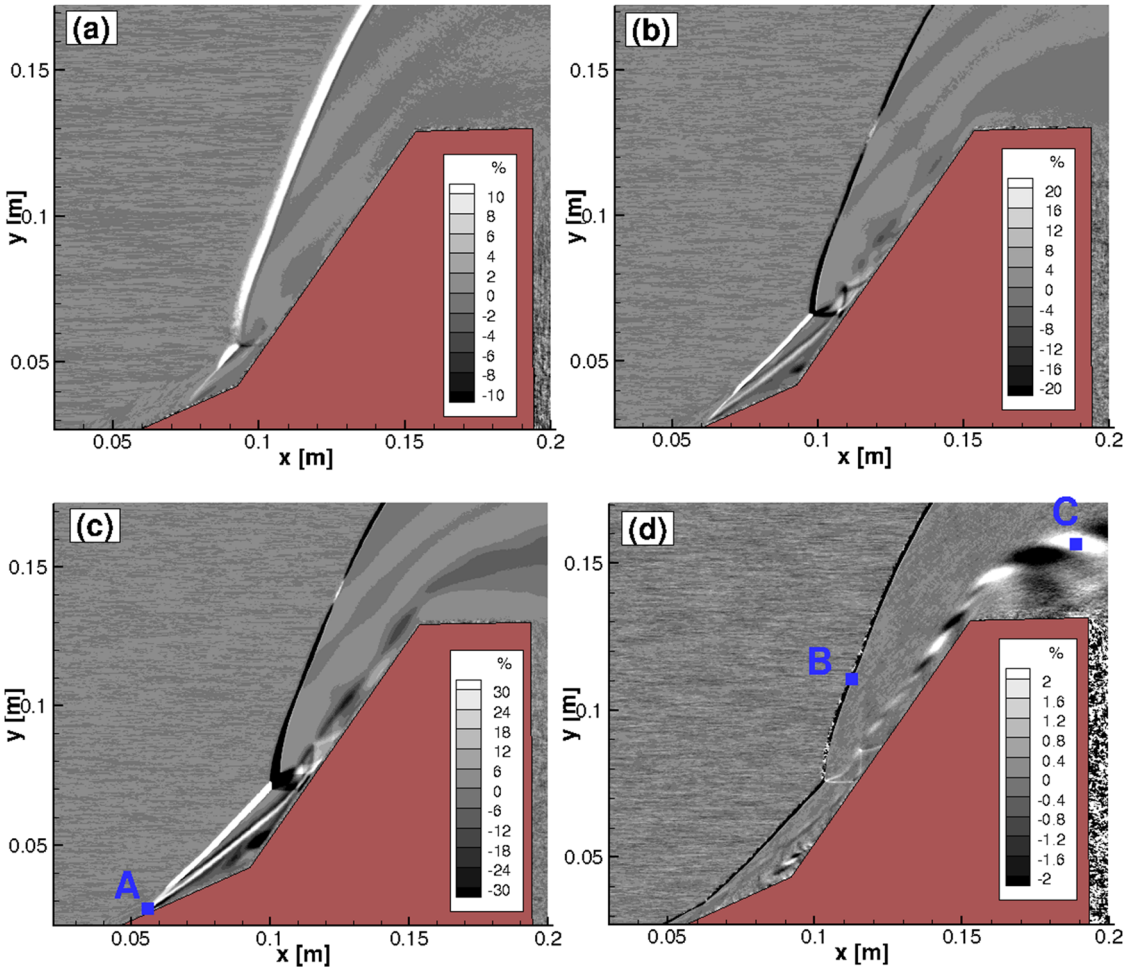

FIG. 13. Percentage difference of the translational temperatures at two different times, $(T_{\text{trn}}(x, y, t_2) - T_{\text{trn}}(x, y, t_1))/((T_{\text{trn}}(x, y, t_2) + T_{\text{trn}}(x, y, t_1))/2) * 100$: (a) for the lowest Re case between, $t_1 = 0.8$ and $t_2 = 2.52$ ms, (b) for the 3X Re case between $t_1 = 1.59$ and $t_2 = 5.31$ ms, (c) for the highest Re case between $t_1 = 1.5$ and $t_2 = 11$ ms, and (d) for the highest Re case between $t_1 = 10.5$ and $t_2 = 11$ ms. Each of the sampled data contains 1000 time step samples after the corresponding specified time steps.

existence of expansion and compression waves seen in the alternative circular regions has a significant effect on the time characteristics of the pressure field, especially for the larger Re number cases. In particular, the magnitude of the alternating maxima and minima pressure circular regions along the second cone surface increases with Reynolds number. Similar to the percentage difference temperature fields shown in Fig. 13, the structure of the λ shocklet is prominent in the pressure field.

The double cone is an axisymmetric shape which has an inherently greater pressure-relief effect compared to the double wedge geometry. We have shown in earlier work that the

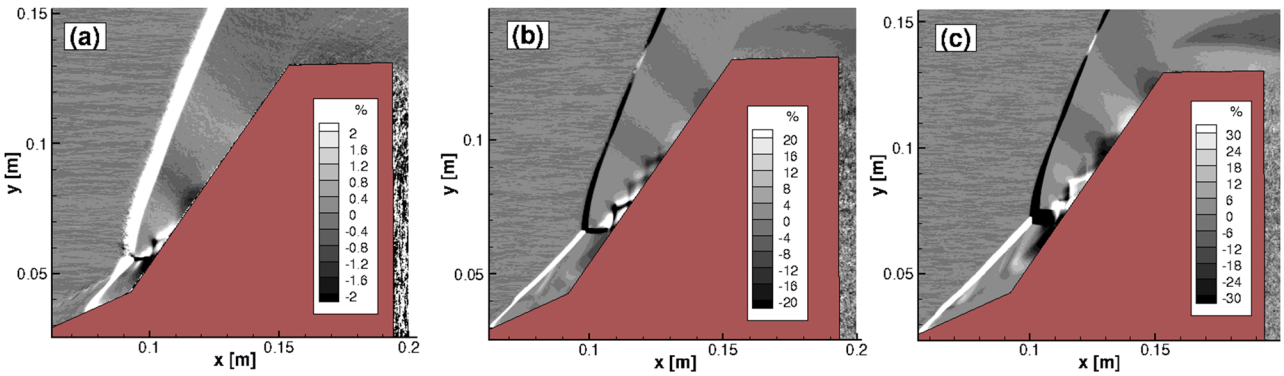

FIG. 14. Percentage difference of the pressure field at two different times, $(P(x, y, t_2) - P(x, y, t_1))/((P(x, y, t_2) + P(x, y, t_1))/2) * 100$, (a) for the lowest Re case between $t_1 = 0.8$ and $t_2 = 2.52$ ms, (b) for the 3X Re case between $t_1 = 1.59$ and $t_2 = 5.31$ ms, (c) for the highest Re case between $t_1 = 1.5$ and $t_2 = 11$ ms.

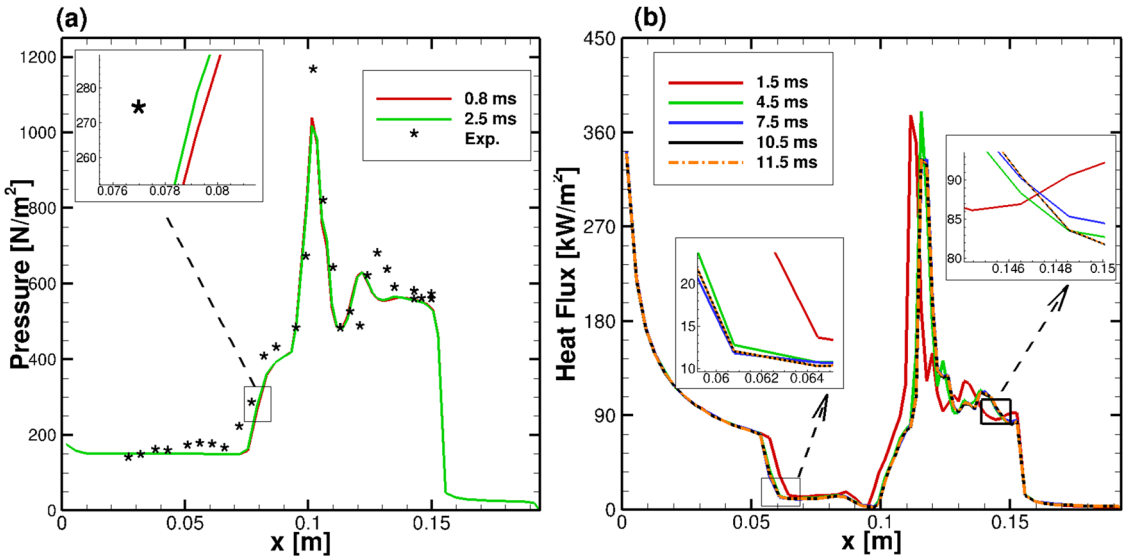

FIG. 15. Time variation of surface parameters: (a) pressure coefficient for the lowest Re case; (b) heat transfer rates for the 4X Re case.

pressure relief effect is important in reducing the size of the separation bubble and hence changes the temporal evolution of the double wedge behavior. Yet these new results for the double cone show for the first time that even for an axisymmetric flow, there is a Reynolds number sufficiently large that the flow will no longer remain stable. Future work will investigate further the cause of this unsteadiness in terms of the identification of new modes that evolve at later times.

Because all ground based experiments have a finite measurement time, understanding the time history behavior of surface parameters is also important. As seen in Figs. 13 and 14, the larger magnitudes of the percentage difference, especially in the separation region and along the second cone surface, play a significant role in the time evolution of surface parameters. For those regions where the percentage difference is close to zero, the flow essentially reaches steady state sooner. However, at the locations in the vicinity of the separation region and in the bow shock, especially for the highest Re case, the flow needs longer time to reach steady state. Figure 15(a) shows the time variation of the surface pressure distribution for the low Re case. Since the temperature and pressure percentage differences [Figs. 13(a) and 14(a)] are small for this low Re number case, the two different temporal solutions for surface pressure are essentially the same and are found to be in good agreement with the experimental data[2,26] which had a measurement time of 24 ms. Although the later time solution at 2.5 ms shows an improvement, there is still a small difference between the prediction of the maxima and points along the aft part of the cone that has never been resolved by any simulations presented in the literature. For the higher Re case, however, the surface heat flux distribution, as shown in Fig. 15(b), exhibits a strong time-dependent behavior especially in the vicinity of the separation and aft regions of the cone where the percentage differences were seen to be large. Based on these results, it can be concluded that at higher Re numbers the duration of the experiment should be sufficiently long to measure steady state surface parameters especially in the separation region and the along second surface.

V. SUMMARY AND CONCLUSIONS

Shock-dominated hypersonic flows over a double cone were investigated by using time accurate DSMC to study the complex flow characteristics of laminar SWBLIs for four different Re number cases. Although the separation shock angle was found to be similar for all Re number cases, increasing the Re number generated a larger separation region and the formation of a secondary vortex which significantly changed the shock structure. In particular, for the higher Re number cases, the larger distance between the two contact surfaces and the greater pressure in the TMR region create λ-shocklets. For the first time, velocity distribution functions obtained at different locations in the flow showed the classic bi-modal distribution behavior in the bow shock, but were nearly Maxwellian at locations near the leading edge and separation points. The study of surface parameters such as velocity and temperature-slip, heat flux, and coefficient of friction showed a number of important results. The heat fluxes obtained from the DSMC simulations were found to be in good agreement with experiments at the lowest Re case. The calculated heating rates and skin friction increase with Reynolds number because the boundary layer becomes thinner. By contrast, the velocity and temperature jump values were found to decrease with Reynolds number because of the decrease in the mean free path.

To characterize the unsteady behavior of the double cone flow and its change with Reynolds number, the residual algorithm was applied to the unsteady DSMC signal to obtain the average damping rate and amplitude function that corresponds to the least damped eigenmode. It was found that as Reynolds number increased, the magnitude of the decay rate decreased, which in turn increases the required simulation time to reach a steady state. For all Reynolds numbers except the 4X case, the time evolution of all flow quantities such as velocities, temperatures, and pressures could be fit by a single eigenmode; however, this becomes less successful at the highest Reynolds number case. Comparing DSMC solutions at two

different times, the temperature field, the separation region, the bow and separation shocks, and the contact surfaces showed more time dependency in comparison to other regions of the flow. The further increase in the Reynolds number resulted in more prominent λ-shocklet structures and a Kelvin-Helmholtz instability arising in the shear layer. In fact for the 4X Re case, the flow does not reach steady state, even though the DSMC simulation was run longer than the typically available 1-2 ms run time of current facilities.[48] The DSMC signal will be used to study the evolution of new modes, some perhaps not decaying, and the critical Reynolds number where transition occurs will be determined.

ACKNOWLEDGMENTS

The research of O.T. and D.A.L. is being supported by the Air Force Office of Scientific Research through AFOSR Grant No. FA9550-11-1-0129 with a subcontract Award No. 2010-06171-01 to UIUC. O.T. and D.A.L. are also grateful for the computational resource provided on ERDC Topaz, AFRL Spirit and Thunder. The work of V.T. is sponsored by the Air Force Office of Scientific Research, Air Force Material Command, USAF, under Grant No. FA9550-15-1-0387 *Global transient growth mechanisms in high-speed flows with application to the elliptic cone*, and Grant No. FA9550-17-1-0115 *Global Modal and Non-Modal Instability Analyses of Shock-Induced Separation Bubbles*, with V.T. as Principal Investigator and Dr. Ivett Leyva as Program Officer.

[1] D. R. Chapman, D. M. Kuehn, and H. K. Larson, "Investigation of separated flows in supersonic and subsonic streams with emphasis on the effect of transition," NACA TN-3869, 1957.
[2] M. S. Holden, T. P. Wadhams, G. V. Candler, and J. K. Harvey, "Measurements in regions of low density laminar shock wave/boundary layer interaction in hypervelocity flows and comparison with Navier-Stokes predictions," AIAA Paper 2003-1131, 2003.
[3] A. B. Swantek and J. M. Austin, "Heat transfer on a double wedge geometry in hypervelocity air and nitrogen flows," AIAA Paper 2012-0284, 2012.
[4] D. H. Rudy, J. L. Thomas, A. Kumar, P. A. Gnoffo, and S. R. Chakravarthy, "Computation of laminar hypersonic compression-corner flows," AIAA J. **29**, 1108–1113 (1991).
[5] J. Olejniczak, M. J. Wright, and G. V. Candler, "Numerical study of inviscid shock interactions on double-wedge geometries," J. Fluid Mech. **352**, 1–25 (1997).
[6] A. S. Durna, M. E. H. A. Barada, and B. Celik, "Shock interaction mechanisms on a double wedge at Mach 7," Phys. Fluids **28**, 096101 (2016).
[7] A. Khraibut, S. L. Gai, L. M. Brown, and A. J. Neely, "Laminar hypersonic leading edge separation—A numerical study," J. Fluid Mech. **821**, 624–646 (2017).
[8] L. Vanstone, D. Estruch-Samper, and B. Ganapathisubramani, "Establishment times of hypersonic shock-wave/boundary-layer interactions in intermittent facilities," AIAA J. **55**, 2875–2887 (2017).
[9] D. V. Gaitonde, P. W. Canupp, and M. S. Holden, "Heat transfer predictions in a laminar hypersonic viscous/inviscid interaction," J. Thermophys. Heat Transfer **16**, 481–489 (2002).
[10] M.-C. Druguet, G. V. Candler, and I. Nompelis, "Effects of numerics on Navier-Stokes computations of hypersonic double-cone flows," AIAA J. **43**, 616–623 (2005).
[11] G. A. Bird, *Molecular Gas Dynamics and the Direct Simulation of Gas Flows* (Clarendon Press, Oxford, England, UK, 1994).
[12] B. E. Edney, "Effects of shock impingement on the heat transfer around blunt bodies," AIAA J. **6**, 15–21 (1968).
[13] H. Babinsky and J. K. Harvey, *Shock Wave-Boundary-Layer Interactions* (Cambridge University Press, 2011).
[14] C. Windisch, B. U. Reinartz, and S. Müller, "Investigation of unsteady Edney type IV and VII shock–shock interactions," AIAA J. **54**, 1846–1861 (2016).
[15] G. Ben-Dor, E. Vasilev, T. Elperin, and A. Zenovich, "Self-induced oscillations in the shock wave flow pattern formed in a stationary supersonic flow over a double wedge," Phys. Fluids **15**, L85–L88 (2003).
[16] P. W. Duck, D. G. Lasseigne, and M. Hussaini, "On the interaction between the shock wave attached to a wedge and freestream disturbances," Theor. Comput. Fluid Dyn. **7**, 119–139 (1995).
[17] A. Fedorov, "Transition and stability of high-speed boundary layers," Annu. Rev. Fluid Mech. **43**, 79–95 (2011).
[18] O. Tumuklu, D. A. Levin, and J. M. Austin, "Shock-shock interactions for a double wedge configuration in different gases," AIAA Paper 2015-1520, 2015.
[19] J. Moss, S. O'Byrne, N. Deepak, and S. Gai, "Simulations of hypersonic, high-enthalpy separated flow over a 'tick' configuration," AIP Conf. Proc. **1501**, 1453–1460 (2012).
[20] O. Tumuklu, Z. Li, and D. A. Levin, "Particle ellipsoidal statistical Bhatnagar–Gross–Krook approach for simulation of hypersonic shocks," AIAA J. **54**, 3701–3716 (2016).
[21] V. Theofilis, S. Hein, and U. Dallmann, "On the origins of unsteadiness and three-dimensionality in a laminar separation bubble," Philos. Trans. R. Soc., A **358**, 3229–3246 (2000).
[22] V. Theofilis and T. Colonius, "An algorithm for the recovery of 2- and 3-D BiGlobal instabilities of compressible flow over 2-D open cavities," AIAA Paper 2003-4143, 2003.
[23] F. Gomez, S. Le Clainche, P. Paredes, M. Hermanns, and V. Theofilis, "Four decades of studying global linear instability: Progress and challenges," AIAA J. **50**, 2731–2743 (2012).
[24] J. N. Moss, "DSMC computations for regions of shock/shock and shock/boundary layer interaction," AIAA Paper 2001-1027, 2001.
[25] J. N. Moss and G. A. Bird, "Direct simulation Monte Carlo of hypersonic flows with shock interactions," AIAA J. **43**, 2565–2573 (2005).
[26] M. S. Holden and T. P. Wadhams, "Code validation study of laminar shock/boundary layer and shock/shock interactions in hypersonic flow. Part A: Experimental measurements," AIAA Paper 2001-1031, 2001.
[27] M. Ivanov, D. Zeitoun, J. Vuillon, S. Gimelshein, and G. Markelov, "Investigation of the hysteresis phenomena in steady shock reflection using kinetic and continuum methods," Shock Waves **5**, 341–346 (1996).
[28] A. Manela and J. Zhang, "The effect of compressibility on the stability of wall-bounded Kolmogorov flow," J. Fluid Mech. **694**, 29–49 (2012).
[29] A. Manela and N. Hadjiconstantinou, "Gas-flow animation by unsteady heating in a microchannel," Phys. Fluids **22**, 062001 (2010).
[30] A. Manela and I. Frankel, "On the Rayleigh–Bénard problem in the continuum limit," Phys. Fluids **17**, 036101 (2005).
[31] M. A. Gallis, T. Koehler, J. R. Torczynski, and S. J. Plimpton, "Direct simulation Monte Carlo investigation of the Rayleigh-Taylor instability," Phys. Rev. Fluids **1**, 043403 (2016).
[32] W. G. Vincenti and C. H. Kruger, Jr., *Introduction to Physical Gas Dynamics* (John Wiley and Sons, Inc., New York, 1965).
[33] M. S. Ivanov, G. N. Markelov, and S. G. Gimelshein, "Statistical simulation of reactive rarefied flows–numerical approach and applications," AIAA Paper No. 98-2669, 1998.
[34] M. S. Ivanov and S. V. Rogasinsky, "Analysis of the numerical techniques of the direct simulation Monte Carlo method in the rarefied gas dynamics," Russ. J. Numer. Anal. Math. Modell. **3**, 453–466 (1988).
[35] P. S. Larsen and C. Borgnakke, "Statistical collision model for Monte Carlo simulation of polyatomic gas mixture," J. Comput. Phys. **18**, 405–420 (1975).
[36] R. C. Millikan and D. R. White, "Systematics of vibrational relaxation," J. Chem. Phys. **39**, 3209–3213 (1963).
[37] J. G. Parker, "Rotational and vibrational relaxation in diatomic gases," Phys. Fluids **2**, 449–462 (1959).
[38] F. E. Lumpkin, B. L. Haas, and I. D. Boyd, "Resolution of differences between collision number definitions in particle and continuum simulations," Phys. Fluids A **3**, 2282–2284 (1991).
[39] N. E. Gimelshein, S. F. Gimelshein, and D. A. Levin, "Vibrational relaxation rates in the direct simulation Monte Carlo method," Phys. Fluids **14**, 4452–4455 (2002).
[40] O. Tumuklu, D. A. Levin, and V. Theofilis, "On the temporal evolution in laminar separated boundary layer shock-interaction flows using DSMC," AIAA Paper 2017-1614, 2017.
[41] J. D. Anderson, *Modern Compressible Flow: With Historical Perspective* (McGraw-Hill, New York, 1990), Vol. 12.
[42] W. He, R. S. Gioria, J. M. Pérez, and V. Theofilis, "Linear instability of low Reynolds number massively separated flow around three NACA airfoils," J. Fluid Mech. **811**, 701–741 (2017).

[43]O. Tumuklu, D. A. Levin, S. F. Gimelshein, and J. M. Austin, "Factors influencing flow steadiness in laminar boundary layer shock interactions," AIP Conf. Proc. **1786**, 050005 (2016).
[44]T. Gökçen, R. MacCormack, and D. R. Chapman, "Computational fluid dynamics near the continuum limit," AIAA Paper No. 87-1115, 1987.
[45]V. Theofilis, "On steady–state flow solutions and their nonparallel global linear instability," in *8th European Turbulence Conference, June 27–30, 2000*, edited by C. Dopazo (International Center for Numerical Methods in Engineering, Barcelona, Spain, 2000), pp. 35–38.
[46]S. Navarro-Martinez and O. Tutty, "Numerical simulation of Görtler vortices in hypersonic compression ramps," Comput. Fluids **34**, 225–247 (2005).
[47]J.-P. Dussauge, P. Dupont, and J.-F. Debiève, "Unsteadiness in shock wave boundary layer interactions with separation," Aerosp. Sci. Technol. **10**, 85–91 (2006).
[48]M. S. Holden, T. P. Wadhams, M. G. MacLean, and A. T. Dufrene, "Measurements of real gas effects on regions of laminar shock wave/boundary layer interaction in hypervelocity flows for 'blind' code validation studies," AIAA Paper 2013-2837, 2013.